Analysis of Structure and Polymorphism in Poly(*p*-phenyleneterephthalamide) through Correlation of Simulation and Experiment

G. C. Rutledge and U. W. Suter*

Department of Chemical Engineering, Massachusetts Institute of Technology, Cambridge, Massachusetts 02139, and Institut für Polymere, Eidgenössische Technische Hochschule, CH-8092 Zürich, Switzerland

C. D. Papaspyrides

Laboratory for Special Chemical Technology, Department of Chemical Engineering, National Technical University of Athens, Athens 106 82, Greece

Received June 28, 1990; Revised Manuscript Received October 9, 1990

ABSTRACT: The study of microstructure in the rigid-rod aramid poly(*p*-phenyleneterephthalamide) (PPTA) is augmented through the correlation of experimentally determined X-ray diffraction patterns with results from an atomistic model designed to simulate pseudocrystalline polymeric materials. Aspects of fiber spinning and X-ray analysis of experimental fibers are presented for comparison with predicted diffraction patterns made possible by atomistic simulation of PPTA. The predicted patterns are derived from PPTA structures having minimum potential energy. The polymorphic nature of the solid-state structure of PPTA is supported by both calculations and experimental X-ray scattering. In comparison with deduced crystal structures reported in the literature, the simulations suggest a low-energy structure readily identified with modification I, also witnessed in the annealed fiber data. The occurrence of modification II is consistent in part with the prediction of several closely related but distinguishable polymorphs having alternate packings of sheets of hydrogen-bonded chains.

I. Introduction

We have presented previously an atomistic modeling method that is applicable to the general study of polymers in a highly ordered, but not necessarily classically crystalline, state.[1] This method has the advantage of generality of application both to ideal crystal structures and to imperfect crystalline structures such as those encountered in highly constrained polymer systems. Our interest in such models stems from our current study of structure–property relationships in engineered rigid-rod polymers. As such, our method has been developed primarily with an interest in application to the case of poly(*p*-phenyleneterephthalamide) (PPTA) and its family of derivatives; in the previous paper, we develop the general description of the model and illustrate its application to the study of PPTA, one of the simplest materials in this family of polymers and one for which there exists considerable structural information in the literature. The simulation analysis elucidates the magnitude and specificity of critical components of the cohesive forces and suggests evidence for the occurrence of polymorphism in the solid state of this rigid-rod aramid. In this paper we present some of the experimental observations from our laboratory concerning the occurrence of microstructure in fibers of PPTA produced via the conventional dry-jet wet-spinning process. The experimental results are interpreted with respect to phenomenological predictions made possible by the molecular simulation as well as results available from the literature.

Since it was first reported by Kwolek[2] in 1972 PPTA has received considerable attention; for a comprehensive summary of the public knowledge to date, the reader is directed to several reviews.[3-5] The scientific and commercial appeal of this and similar materials lies in their liquid crystal phase behavior, high thermal stabilities, and high tensile moduli and strengths when processed into fiber form.[6] The thermal characteristics are credited to the high aromaticity content of the polymer chain and the high density of hydrogen bonding anticipated in the solid state. The high-performance tensile properties of these aramid fibers are commonly attributed to the unusually stiff extended conformational characteristics of the molecules and the relative ease with which these macromolecular chains may be aligned along the fiber axis during fiber formation. π-Bonding electron orbitals above and below the plane of the phenylene ring and the conjugated double-bond character of the carbon–nitrogen and carbon–oxygen bonds in the amide link lend structural rigidity to the individual backbone moieties; thus molecular flexibility is possible only through rotation about bonds connecting successive moieties. The barrier to rotation and chain folding about the amide bond is on the order of 20 kcal/mol, with only a rare occurrence of cis conformations.[7,8] Rotation about the bonds connecting successive phenylene rings and amide groups is also restricted by the energetically advantageous tendency toward electron delocalization realized when these moieties are coplanar, on the one hand, and repulsive overlap of atomic spheres, on the other. furthermore, such rotation produces little conformational change when the chain-extending bonds on the ring are in the para positions. As such, these polymers resemble wormlike chains in solution, with typical persistence lengths on the order of 150–250 Å.[9-11]

The lack of conformational flexibility and high degree of chain extension have two important ramifications. First, a relatively limited number of additional conformations are available to the polymer in solution or melt over that available in the solid state; for this reason, the entropies of solution and melting are expected to be unusually small. This contributes to the characteristically high melting points of aramids, on the order of 500+ °C; these polymers typically undergo decomposition concurrent with or prior

* To whom correspondence should be addressed at the Institut für Polymere, Eidgenössische Technische Hochschule.

0024-9297/91/2224-1934$02.50/0

to melting. As such, they must be processed from lyotropic phases. However, since dissolution is little aided by entropic effects, the solubility of these aramids is largely determined by the enthalpies of dissolution. PPTA, for example, is only soluble in highly aggressive polar solvents, such as concentrated sulfuric acid, making processing difficult and expensive. Second, above a critical concentration the polymer forms a stable anisotropic solution mesophase. This ordered-phase formation in aramids has been anticipated through the use of lattice models predicting nematic liquid crystal phase formation for monodisperse and polydisperse rods.[12-15] Experimental studies on PBA, PPTA, and some of their chlorinated derivatives in dilute solution confirm the extended conformations on these chains.[9,11,16,17]

II. Previous Work

Processing Aspects. Aramids have been processed into both film and fiber form by means of solvent/nonsolvent exchange. For the formation of highly oriented, pseudocrystalline morphologies, the dry-jet wet-spinning process described by Blades[18,19] represents the best means currently available. By this process, the polymer in solution is extruded first through a "dry zone" prior to entry into the coagulation bath. While isotropic spin dopes may be used, the highest degrees of molecular orientation require the use of a liquid crystal solution dope. These domains may be conveniently oriented on a molecular scale prior to solidification.[20-23] Without preorientation in solution, the long relaxation time for polymer motion prevents adequate molecular orientation within the time frame of the spinning process.[24] An extensional flow gradient, which is most pronounced in the dry zone, is realized by collecting the precipitated fiber at a greater linear velocity than that at which the solution exits the spinning die; increasing the extensional flow field improves the degree of orientation along the major axis of the fiber.[25] In the coagulation bath, a shear gradient is created due to the differential between filament and coagulant flow velocities, which may be reduced by providing for concurrent coagulent flow in the vicinity of the fiber. Depending on the relative solvency strengths and diffusivities of the solvent and coagulant, a skin layer may form on the fiber, resulting in a differentiation between a fiber "skin", wherein solidification has occurred most rapidly, and a fiber core, where solidification and crystallization proceed more slowly and to greater perfection. Thus the final morphology may be affected by changes in many processing factors, such as solution and coagulant temperatures, residence time and relaxation time of the solution/solid mixture in each zone, shear rates at the spin die and in the bath, the magnitude and distribution of extensional stresses along the fiber path, and the evolution of polymer/solvent/nonsolvent composition along the spin line.

Postspin heat treatments near the melt temperature may provide the chains with sufficient mobility in the solid state to "melt out" kinetically frozen crystal forms in favor of the thermodynamically most favorable form. A significant jump in tensile modulus follows upon heat treatment and the average molecular weight increases due to end-linking of chains.[25] Tenacity and modulus both increase with decreases in orientation angle, a measure of the crystallite misalignment obtained through X-ray diffraction analysis. Orientation is improved by increased solution anisotropy in the quiescent state or by an increased extensional flow gradient during solidification. The resulting fibers are conjectured to bear tensile loads almost entirely along the molecular axis, which, being fully extended, may not elongate significantly without bond scission.

Table I
Crystallographic Parameters of Previously Reported Modifications of PPTA

	modification I[a,c]	modification II[b,c]
a, Å	7.87	8.0
b, Å	5.18	5.1
c, Å	12.9	12.9
γ, deg	90	90
chain locations	[0,0]; [1/2,1/2]	[0,0]; [1/2,0]
no. of H_2SO_4	—	—
space group	Pn or $P2_1n$	Pa or $P2_1a$
density, g/cm^3	1.50	1.50

[a] Northolt, 1974. [b] Haraguchi et al., 1979. [c] Monoclinic cell type.

Solid-State Morphology. Previous investigators have reported on the considerable structural complexity of fibrous PPTA.[26-28] For length scales greater than tens of nanometers, one speaks of a supramolecular structure composed of superposed periodic defect layers (35-nm period) and radially oriented sheet structures with periodic pleats (500-nm period), microfibrillar morphology (600-nm diameter), and skin–core differentiation; recently, Kevlar 149 has been reported to exhibit a higher degree of crystallinity and crystallite size and to be devoid of both pleat and microfibrillar macromorphologies as well as of skin–core differentiation.[5] On the molecular scale, chain ordering has been portrayed by using crystalline and paracrystalline descriptions. Correlations of the breadths of meridional X-ray diffraction peaks with the square of reflection order, as predicted by a one-dimensional paracrystal model having distortions of the second kind, and with tensile modulus have been used to suggest a distorted lattice paracrystalline structure in PPTA.[29-31] In addition to unusual chain rigidity, the aramids experience strong intermolecular cohesive forces in the solid state due to interactions between the polar amide moieties on neighboring chains. This cohesive ability presumably improves the mechanical properties of the bulk polymer transverse to the axis of orientation, for resistance to shear and compressive failure, and leads to high thermal stability; however, this strong cohesion also causes the chains to associate and reduces the enthalpic driving force for mixing, thus contributing to the poor solubility of the polymer.

Other investigators have suggested that PPTA may coexist in several packing modes, or polymorphs.[20,32-34] To date, two different but related polymorphs for the pure polymer[32,33] have been isolated and identified through the use of conventional X-ray analytical techniques. The unit cell descriptions for each of the pure polymer structures are listed in Table I. In the first, denoted modification I, the derived unit cell is pseudoorthorhombic with two chains per unit cell; this structure is shown in Figure 1a. The chain conformation is fully extended with ring rotation angles of −30 and +38°. The chains are rotated about their axes such that the amide planes lie 4° out of the bc crystallographic facet. The second polymorph, denoted modification II and shown in Figure 1b, was derived as a variation of modification I. Here, the same chain conformation is maintained, with location of the second chain shifted from [1/2,1/2] in the ab facet to [1/2,0]; however, the resolution of the scattering data in this case was insufficient to determine a unique setting angle. The occurrence of the two polymorphs results from the different environments in which each is coagulated and the ability of the coagulant to interfere with interchain hydrogen bonding during solidification.[33] Under certain conditions

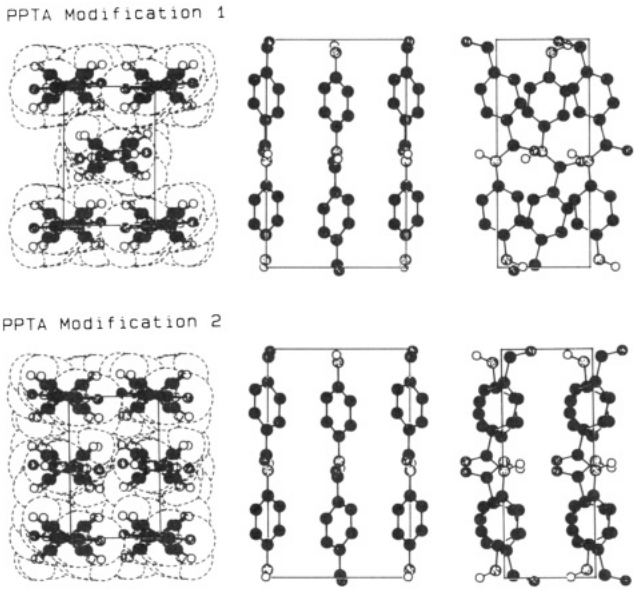

Figure 1. The two reported crystal structures for poly(*p*-phenyleneterephthalamide): (a) modification I (Northolt, 1974); (b) modification II (Haraguchi et al., 1979).

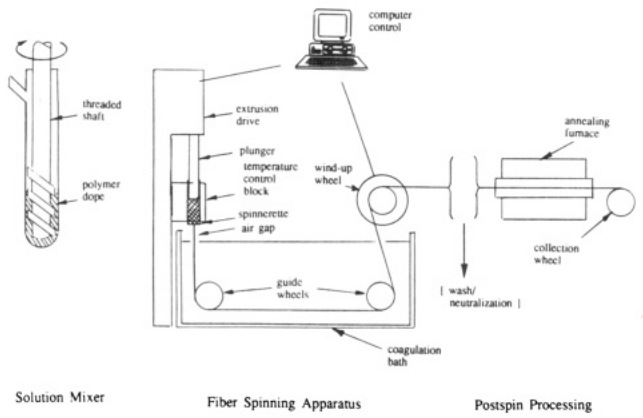

Figure 2. Schematic of the experimental program for polymer dissolution, fiber spinning, and postspin heat treatment.

modification II may transfer to modification I upon annealing.

III. Experimental Methods

Dope Preparation. Our PPTA solutions consisted exclusively of Kevlar 29, supplied by E. I. du Pont de Nemours and known to consist primarily of PPTA,[35,36] redissolved in 100% H_2SO_4. The inherent viscosity of the polymer was 6.1 dL/g in 96% H_2SO_4 (determined with an Ostwald viscometer and a standard concentration of 0.05 g of polymer in 10 mL of solvent) at 25 °C. With the assumption that at concentrations of 0.5 g/dL $\eta_{inh} \approx [\eta]$ and with Mark–Houwink constants of $K = 8 \times 10^{-5}$ dL/g and $a = 1.09$,[9] this corresponds to an approximate molecular weight of 30 000 (DP ≈ 240). The spin dopes were prepared by combining the polymer staple with solvent under an inert atmosphere, heating to 60–80 °C, and thoroughly mixing by slow stirring (i.e. ≤60 rpm) using a threaded screw mixer, illustrated in Figure 2. Concentrations from 4.0 to 17.5 wt % were made. The formation of an anisotropic phase occurs at ca. 7–8 wt % polymer in sulfuric acid at 25 °C; for most trials, a solution of 10 wt % polymer in solvent was used. Change in molecular weight due to shear-induced degradation or thermal decomposition was checked by viscometry and found to be insignificant. Anisotropy was confirmed by stir opalescence and polarized light microscopy.

Fiber Formation. A dry-jet wet-spinning apparatus as shown in Figure 2 was constructed for the conversion of anisotropic dope to fiber. Approximately 5 mL of the polymer dope was prefiltered and homogenized as it was loaded to the syringe by means of a prefilter attachment. The dope was then extruded through the die orifice by using a motor-driven plunger. Spinnerette die diameters from 60 up to 120 μm were used, but the 60-μm dies were preferred. (Our spinnerette geometries were generally specified with a 1:1 length to diameter ratio, but the capillary length was not confirmed in all cases.) Operative filament velocities at the orifice ranged from 5 to 80 m/min, depending upon plunger rate and orifice diameter; 40 m/min was typical. The filament passed initially through an air gap of 5–10 mm and then through the aqueous coagulation bath at room temperature (24 °C) along a path length on the order of 105 cm at ambient temperature. Finally, the precipitated polymer filament was collected on the wind-up roller, whose rotation speed was selected relative to the linear velocity of the plunger to induce draw-down of the filament. The collected fiber sample was then washed in water, followed by neutralization overnight of residual acid in a 1 wt % NaOH solution bath, followed in turn by a final water wash and drying at 60–80 °C. This constitutes the denoted "as-spun" fiber.

Heat Treatment. The sample was drawn through a high-temperature zone under an inert atmosphere one or more times to produce the denoted "annealed" fiber. A residence time of 2 s at 500 °C was employed, in accordance with recommendations in the literature.[2,37] Subsequent annealing passes did not appear to alter the structural characteristics observed by X-ray analysis to any significant extent.

IV. Spinning Trials for PPTA

The primary factor effecting molecular orientation during the spinning process is the draw-down ratio D_R, a measure of the extensional flow field acting to orient the nematic domains. We generally quote a nominal draw-down ratio, or spin-stretch factor, based on the known extrusion and wind-up velocities. The actual extensional flow field depends upon the true draw-down ratio, which is augmented by the tendency for the extruded filament to swell as it exists the spinnerette; this swelling is caused by the relaxation upon transition from confined to free surface flow of residual stresses imposed upon the extrudate by flow through the die geometry. In the range of shear rate γ_w, defined as in eq 1

$$\gamma_w = 8v_e/D_{orifice} \tag{1}$$

for an incompressible Newtonian fluid, from 6000 to 17 200 s^{-1}, Conio et al.[23] found die swell in poly(*p*-benzamide) (BPA; η_{inh} of 1.37 and 1.85 dL/g) to increase from 1 at very low extrusion speeds up to 1.3 at an extrusion speed of 13 m/min. Jaffe and Jones[38] report a linear correlation between the logarithms of die swell and shear rate at the wall for PPTA; in the range γ_w = 25 000–90 000 s^{-1}, die swell varied from roughly 1.1 up to 1.7. In this investigation, using a 10 wt % solution of polymer in 100% H_2SO_4 spun at 30 °C, we determined that wind-up velocity necessary to match exactly the linear velocity of the swollen filament. Under the assumption that the filament does not undergo additional dimensional changes, other than those due to relaxation, before the collection roller, we may calculate the die swell as the square root of the ratio of linear velocities, as indicated in eq 2. We obtain values for the shear rate and shear stress at the wall of the die using eqs 1 and 3, respectively:

$$\text{die swell} = (v_e/v_w)^{1/2} \tag{2}$$

$$\tau_w = D_{orifice}P/4L_{orifice} \tag{3}$$

P refers to the driving pressure for extrusion, assumed to be equal to the force per unit area at the end of the moving plunger. Figure 3 shows the variation of die swell and shear stress with shear rate in the range 30 000 < γ_w < 185 000 s^{-1} for our apparatus using a spinnerette of diameter 60 μm and capillary length of 100 μm and a 10

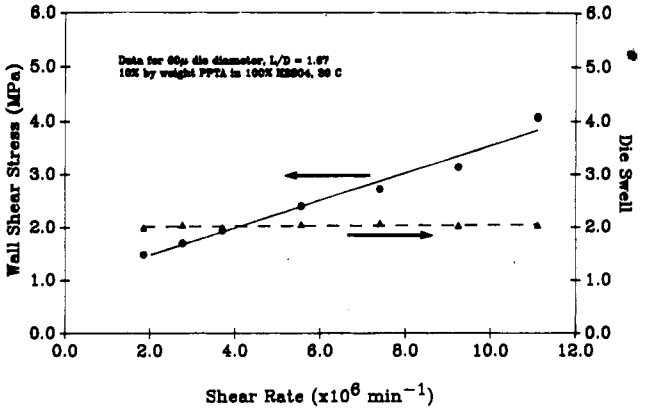

Figure 3. Shear stress at the wall and die swell as functions of shear rate at the wall for the spinning of PPTA from a 10 wt % solutions in 100% H_2SO_4 at 30 °C using a spinnerette of diameter 60 μm and capillary length 100 μm.

Table II
Summary of Selected Fiber-Spinning Trials

	nominal draw-down ratio	dry-fiber diam, μm	orientation angle, deg as spun [annealed]
trial 1			
polym concn = 10 wt %	0.3	28	66
extrusion temp = 30 °C	0.5	23	43
extrusion rate = 31 m/min			
spinnerette diam = 55 μm			
die swell = 2.0			
trial 2			
polym concn = 10 wt %	1.3	38	63 [46]
extrusion temp = 25 °C	2.0	24	34 [28]
extrusion rate = 36 m/min	2.6	21	20 [20]
spinnerette diam = 60 μm	2.9	22	25 [20]
die swell unknown	3.2	22	20 [22]
trial 3			
polym concn = 17.5 wt %	0.9	35	46
extrusion temp = 80 °C	1.2	32	32
extrusion rate = 30 m/min	1.7	24	30
spinnerette diam = 63 μm			
die swell = 1.3			
trial 4			
polym concn = 17.5 wt %	1.0	31	36
extrusion temp = 80 °C	1.7	25	33
extrusion rate = 60 m/min	2.0	22	35
spinnerette diam = 63 μm	2.5	19	31
die swell = 1.3	3.0	18	31

wt % polymer dope. Die swell remains essentially constant over the range of shear rates employed in this work, while shear stress increases almost linearly with shear rate. The shear-thinning behavior under these conditions is considerably less pronounced than that reported by Aoki et al.[16] for a similar dope at 25 °C; however, the shear rates employed here are considerably higher than those reported by Aoki et al. The die swell is somewhat larger than that observed by other investigators; this is probably due to differences in the extrusion geometry and the imposition and relaxation of applied stresses prior to the extruder exit. Conio et al. suggest that this effect should decrease with increasing polymer concentration and higher extrusion temperatures. In agreement with these observations, using a 17.5 wt % solution of PPTA in 100% H_2SO_4 spun at 80 °C through the same orifice (i.e., 60 μm × 100 μm), we observe a die swell of only 1.3 in the range 37 000 < γ_w < 127 000 s^{-1}.

Table II summarizes some results of variations in draw-down ratio. Here we adhere to the use of nominal draw-down ratios and report the estimated die swell where possible. The trends are consistent with those suggested in the literature for the related polymer PBA.[25] Specifically, we note that fiber radius decreases with increasing draw-down ratio for as-spun fiber, consistent with dimensional changes normally accompanying extensional flow. Orientation angle, determined as the azimuthal breadth at half the maximum intensity of the X-ray diffraction peak at $2\theta = 22.5°$, decreases with increasing draw-down ratio for as-spun fiber; this is in line with expectations for alignment of nematic domains upon exposure to linear accelerations after leaving the spinnerette. Our annealing method produces no measurable dimensional change in the fiber but results in a decreased orientation angle for those fibers initially spun at low draw-down ratio. At higher draw-down ratios we observe a limiting orientation angle that is actually lower (i.e., better alignment) for the 10 wt % polymer dope. A similar limit in fiber properties is reported by Valenti et al.[22] for modulus as a function of draw-down ratio for their work on X-500, the polyterephthalamide of *p*-aminobenzhydrazide, with a break occurring near $D_R = 1.5$. The ultimate orientation angle values are comparable to values reported in the literature. Hindeleh et al.[31] report values of 12.4 and 18.9° for commercial Kevlar 49 and Kevlar 29, respectively. This suggests that our process produces representative fibers. Lastly, we mention that we observe no evidence of an amorphous halo in the X-ray diffraction scans for the annealed fiber. Even in the as-spun fiber, adequate reproductions of the diffraction traces were achieved with the consideration solely of the apparent peaks. From this we conclude that our fiber contains at most a very small amorphous fraction.

V. Presentation of WAXS Fiber Diffraction Patterns

Predictions by Simulation. Theoretical wide-angle X-ray scattering (WAXS) reflection intensities are calculated for each of eight isoenergetic structures anticipated by molecular mechanics simulation techniques and reported in the previous paper.[1] It is important to stress here that the calculated structures referred to hereafter are structures of *minimum potential energy*, identified through the simultaneous minimization of intramolecular and intermolecular energies, using interatomic force fields based on first principles, with *no adjustable parameters*. This is in contrast to the crystal structures previously reported in the literature, which were derived by fitting the X-ray scattering patterns from atomic models directly to experimental data; these latter models are not a priori minimum-energy configurations.

We assume the interior unit cell to be representative of the bulk and apply the conventional summation of atomic scattering over lattice indices, *h*, *k*, and *l*, to arrive at the set of structure factors $F(hkl)$, which were then corrected for polarization, Lorentz scattering, and isotropic thermal motion to obtain observable intensities $I_{obs}(hkl)$:[39]

$$I_{obs}(hkl) = M(\theta)\, P(\theta)\, L(hkl)\, |F(hkl)|^2 \qquad (4)$$

$$F(hkl) = \sum_{j=1}^{n} f_j (\sin\theta/\lambda)[\cos(2\pi(hx_j + ky_j + lz_j)) + i\sin(2\pi(hx_j + ky_j + lz_j))] \qquad (5)$$

n is the number of atoms in the unit cell and *h*, *k*, and *l* are the indices defining the crystallographic planes. f_j is the atomic scattering factor, expressed as a function of the Bragg angle θ and the wavelength of radiation, for

atom j located at the fractional coordinate position (x_j,y_j,z_j). The correction factor employed for polarization effects was

$$P(\theta) = (1 + \cos 2\theta)/2 \quad (6)$$

For the Lorentz factor one takes (from de Wolff[40])

$$L(hkl) = (\sin^2\theta \cos\theta \sin\phi)^{-1} \quad \text{for general reflections} \quad (7)$$

$$L(00l) = (t \sin^2\theta \cos\theta)^{-1} \quad \text{for meridional reflections} \quad (8)$$

Here, ϕ is the angle between the normal to the reflecting planes and the fiber axis; t is given to a reasonable approximation in terms of the azimuthal angle $\beta_{1/2}$, in radians, at which the intensity of the reflection falls to half of its peak value (at $\beta = 0°$), by

$$t = 0.815\beta_{1/2} \quad (9)$$

The correction for thermal motion, finally, is

$$M(\theta) = \exp[-8\pi^2\mu_s^2(\sin^2\theta/\lambda^2)] \quad (10)$$

where μ_s^2 is the isotropic mean-square displacement of atoms due to thermal motions, assumed to be the same for all atoms.

For purposes of display, the intensity of each calculated reflection was assumed to be distributed about its mean position according to Gaussian distributions in 2θ and β. The breadths of these distributions represent the expected peak broadening due to finite crystallite sizes, the crystal mosaic, and paracrystal distortions, which are not available a priori from the model calculations. Additionally, we require an estimate for $\beta_{1/2}$ for the Lorentz correction of meridional reflection intensities. The peak-broadening distributions were selected of the form

$$y = A \exp[(-\ln 2)(2(x - x_0)^2/\omega_x^2)] \quad (11)$$

where A is the amplitude of the distribution at x_0 and ω_x is the breadth of the distribution at $y = A/2$. Then the intensity at any point of the diagram may be calculated by summation of the contributions from all reflections at that point; the integrated volume of the distribution in 2θ and β equals the calculated intensity I_{obs} of each reflection i located at $(2\theta_i,\beta_i)$:

$$I_{obs}(hkl) = A_{hkl}\omega_{2\theta}\omega_\beta\pi/4 \ln 2 \quad (12)$$

$$I_{obs}(x_1,x_2) = \sum_{i=1}^{n_p} A_i(\exp\{(-\ln 2)[2(x_1 - 2\theta_i)/\omega_{2\theta}]^2\}) \times (\exp\{(-\ln 2)[2(x_2 - \beta_i)/\omega_\beta]^2\}) \quad (13)$$

We require only three parameters not available through the model, the root-mean-square thermal displacement amplitude and estimates of $\omega_{2\theta}$ and ω_β, in order to recreate the entire fiber diffraction pattern. For our universal isotropic thermal displacement factor we employed the B value used successfully by Northolt[32] for the experimental analysis of scattering from PPTA:

$$B \equiv 8\pi^2\mu_s^2 = 5 \times 10^{-16}\ \text{cm}^2$$

corresponding to a root-mean-square displacement of 0.25 Å. For $\omega_{2\theta}$ and ω_β, values of 1.5 and 15°, respectively, were found to be appropriate, corresponding to $\beta_{1/2} = 7.5°$. At this level of prediction, it was not deemed justified to incorporate anisotropy of the thermal motion correction into the pattern simulations. The simulated fiber diffraction patterns were generated on an IRIS 4D series workstation with GT graphics and a 1280 × 1024 pixel display terminal. The grid density ($2\theta \times \beta$) was 500 point × 450 point per quadrant, or steps of 0.1° in 2θ and 0.2° in β. Visual resolution was enhanced by using a nonproportional gray scale to achieve the greatest visual sensitivity at the lower intensities characteristic of the majority of reflections; a scale is provided in each diffractogram for clarification.

Experimental Data Analysis. We employed WAXS and infrared (IR) absorption techniques for evaluation of the quality of fiber spinning and the concurrence between experimental and simulation results. Two different WAXS apparatuses were used to gather data during the course of this work (Rigaku D4148H2 with nickel-filtered radiation; Siemens D500 with a bent quartz crystal monochromator). Both machines were rotating-anode diffractometers equipped with four-circle goniometers and scintillation counters and employed Cu Kα radiation (λ = 1.5418 Å). Multifilament samples were prepared by embedding the filament ends in epoxy and mounting on a frame suitable for positioning in the incident X-ray beam. Infrared measurements were made with a Mattson Cygnus 100 FTIR apparatus. Samples were prepared from cut fiber cast in potassium bromide at roughly 2% by weight. Measurements were generally made in the range 4000–400 cm^{-1}.

WAXS analysis of the experimental fiber samples proceeded in two stages. The first was an initial evaluation of crystallinity and molecular order by means of equatorial and meridional scans of diffracted intensity versus scattering angle 2θ. This also included a routine scan of diffracted intensity versus azimuthal angle β for a major reflection, generally the intense equatorial reflection at 2θ = 22.5°, for purposes of estimating crystallite orientation within the fiber sample. The second stage entailed the generation of the full two-dimensional fiber diffraction pattern for comparison to simulation results. Scans of intensity versus 2θ were performed in the range 10–55° by steps of 0.1° in 2θ at the desired β. Azimuthal scans were performed in steps of 1 or 2° in β at the desired 2θ. Complete fiber diagrams were re-created from successive radial scans of intensity versus 2θ obtained at different values of β between 0 and 90° and which were then replicated in the remaining three quadrants. Counting times were selected to ensure a signal error level of <5%. The reported intensities were corrected for background radiation and normalized prior to construction of the intensity versus $(2\theta,\beta)$ grid for interpolation and display on the IRIS 4D GT system; all other corrections have already been applied in the calculation of the simulated reflection intensities. The same routines were used to create the visual display as were employed in the cases of the simulated structures; in this manner, comparable fiber diffraction patterns were displayed for both simulated and experimental data sets.

As a further check for experimental accuracy, selected experimental diffraction patterns were analyzed by conventional methods for indexing of significant reflections. The data grids for X-ray diffraction from actual fibers were analyzed quantitatively by selecting a finite number of Gaussian peaks to fit to the two-dimensional experimental pattern, of the same form as were used to display the simulated structure patterns. The fitting procedure was performed through minimization of the relative deviation R_D of the complete pattern intensity distribution as a function of the peak heights A_i, positions $(2\theta_i,\beta_i)$, and

widths at half-intensity ($\omega_{2\theta},\omega_{\beta}$) for all peaks $i = 1$ to n_p.

$$R_D = \frac{\sum_{i=1}^{n2\theta}\sum_{j=1}^{n\beta}(I_{exp,i,j} - I_{calc,i,j})^2}{\sum_{i=1}^{n2\theta}\sum_{j=1}^{n\beta}(I_{exp,i,j})^2} \quad (14)$$

Allowing all parameters to vary independently describes a set of $5n_p$ independent variables; this number was initially limited by requiring all peaks to have the same set of peak widths, reducing the independent parameter set to $3n_p + 2$. The fitting procedure was initiated with different numbers of peaks and different initial peak assignments until a best fit (i.e., minimum relative deviation R_D) was achieved; the variance was generally <10%. Subsequent reoptimization allowing each distribution to vary independently in width did not produce significant improvements in fitting. For the final set of Gaussian peaks describing the best fit to the experimental pattern, the total intensity attributable to each reflection was calculated with eq 12.

VI. Discussion

Evaluation of Simulated Patterns. Due to the nature of the simulation, the calculated structures are inherently triclinic, so that observed reflections are actually groups of reflections of related diffraction planes; the slight displacement of these planes further contributes to the diffuseness of reflections expected in observable patterns and illustrates the potential complexity of reflections whose composite appears as a single "reflection" on film. The composites of reflections are illustrated in the recreated fiber diffractograms presented in Figure 4a–h, corresponding to the eight isoenergetic PPTA structures described previously.

Diagrammatic representations of the calculated X-ray diffraction patterns provide a simple yet effective means for distinguishing between polymorphs at the phenomenological level, both for comparing and contrasting the various results of the model analyses and for later comparison to actual experimental data. For example, common to all the final polymorphs are the intense [002], [004], and [006] meridional reflections, characteristic of the extended-chain conformations and the approximate 2_1 screw symmetry of chains; inclination of the normal to the *ab* facet away from the chain axis results in these reflections appearing slightly off-meridian in a few cases. Only in the fifth, sixth, and eighth structures where translation between neighboring sheets is 2.5–3.0 Å, are weak [001] and [005] meridional reflections observed. Most characteristic of the simulated PPTA patterns is the fingerprint of the equatorial and first layer lines of each structure. Here one can easily distinguish, by means of the presence or absence of [011] or [111] families of reflections (relative to the intense [110] reflection), between structures 1 and 3, having oppositely directed amide dipoles in successive hydrogen-bonded sheets, and structures 2 and 4, having codirected dipoles in successive sheets. Structures 6 and 7, having face-centered unit cells and phenylene rings that are similarly rotated with respect to the amide bonding planes (and hence with respect to the hydrogen-bonded sheets), have characteristically intense second-layer reflections (i.e., [112] or [212] families of reflections).

Comparison to Experimental Patterns. Parts a and b of Figure 5 show reconstructed experimental X-ray diffractograms for our $D_R = 3.2$ fiber (Table II, trial 2) before and after annealing, respectively. Results from the quantitative analysis and deconvolution of peaks are reported in Table III, along with a summary of the reflection identifications reported by Northolt[32] and Haraguchi et al.[33] for modifications I and II, respectively. The as-spun fiber exhibits a poorly resolved diffraction pattern, which is to be expected from a morphology determined primarily by kinetic constraints operative during coagulation. Prior to annealing, the possibility for imperfect crystallinity or multiple coexisting crystalline polymorphs is significantly greater. There is no assurance that such a morphology should consist entirely, or even primarily, of the thermodynamically most stable allomorph. The most notable feature of the as-spun fiber is the appearance of equatorial reflections at 17.9 and 22.6° in 2θ, in agreement with modification II, and of a new equatorial reflection at 27.7°, indicative of an [*hk*0] reflection not previously reported. These reflections are in agreement with a structure possessing chains at the [0,0] and [$^1/_2$,0] locations in the *ab* facet of the unit cell, suggestive of the simulation structures 5–8. The last three of these, structures 6, 7, and 8, all possess similarly rotated phenylene rings with respect to the amide bond plane in the chain conformation, with the resulting generation of significant second-layer nonmeridional reflections. This leaves PPTA structure 5 (Figure 4e, Table IV) as that most consistent with the as-spun fiber. This structure also predicts significant reflections attributable to both [210] and [211] sets of diffraction planes; the former, while not noted by Haraguchi et al. in modification II, is consistent with our as-spun fiber and, in conjunction with the close-lying [211] reflection, reproduces well the intensity previously attributed solely to the [211] planes. The considerable tilt (12°) of the normal to the *ab* facet with respect to the chain axis in the simulated structure 5 also produces a splitting of most of the reflections along the layer lines. However, peak resolution in our as-spun fiber is generally insufficient to justify a more detailed analysis of crystal structure. We do observe that, in agreement with the simulation results, the meridional reflections located at 28.4 and 43.7°, attributable to the [004] and [006] reflections and determined primarily by chain conformation, are indicative of an extended-chain conformation.

Upon annealing we note a structural transformation such as that reported by other investigators.[33,41,42] The equatorial reflections at 17.9 and 27.7° disappear in favor of a strong reflection at 20.5° and an off-equatorial refection at 29.1°, characteristic of modification I. Other strong equatorial refections occur at 25.5 and 38.4°. Only the [111] reflection predicted to occur at 21.7° cannot be resolved in our patterns. Reflections along the meridian shift to 28.0 and 43.4°, indicative of a slight extension of the chains during annealing, but remain consistently higher in 2θ than those reported by Northolt.[32] Intensities of meridional reflections are also lower, but we see increased intensities of off-meridional reflections such as [106] and [104]. The final dominant structure in the annealed fiber agrees well with modification I.

Of the eight polymorphs suggested by simulation, the PPTA structures identified as structures 3 and 4 bear the greatest resemblance to modification I and hence to our annealed fiber. The difference between the two predicted structures lies in the packing of sheets of chains held together by hydrogen bonding between amide moieties. With the exception of the overlap of the intense [200] and [110] reflections in the simulated patterns for PPTA structures 3 and 4 in Figure 4c and d, the agreement in

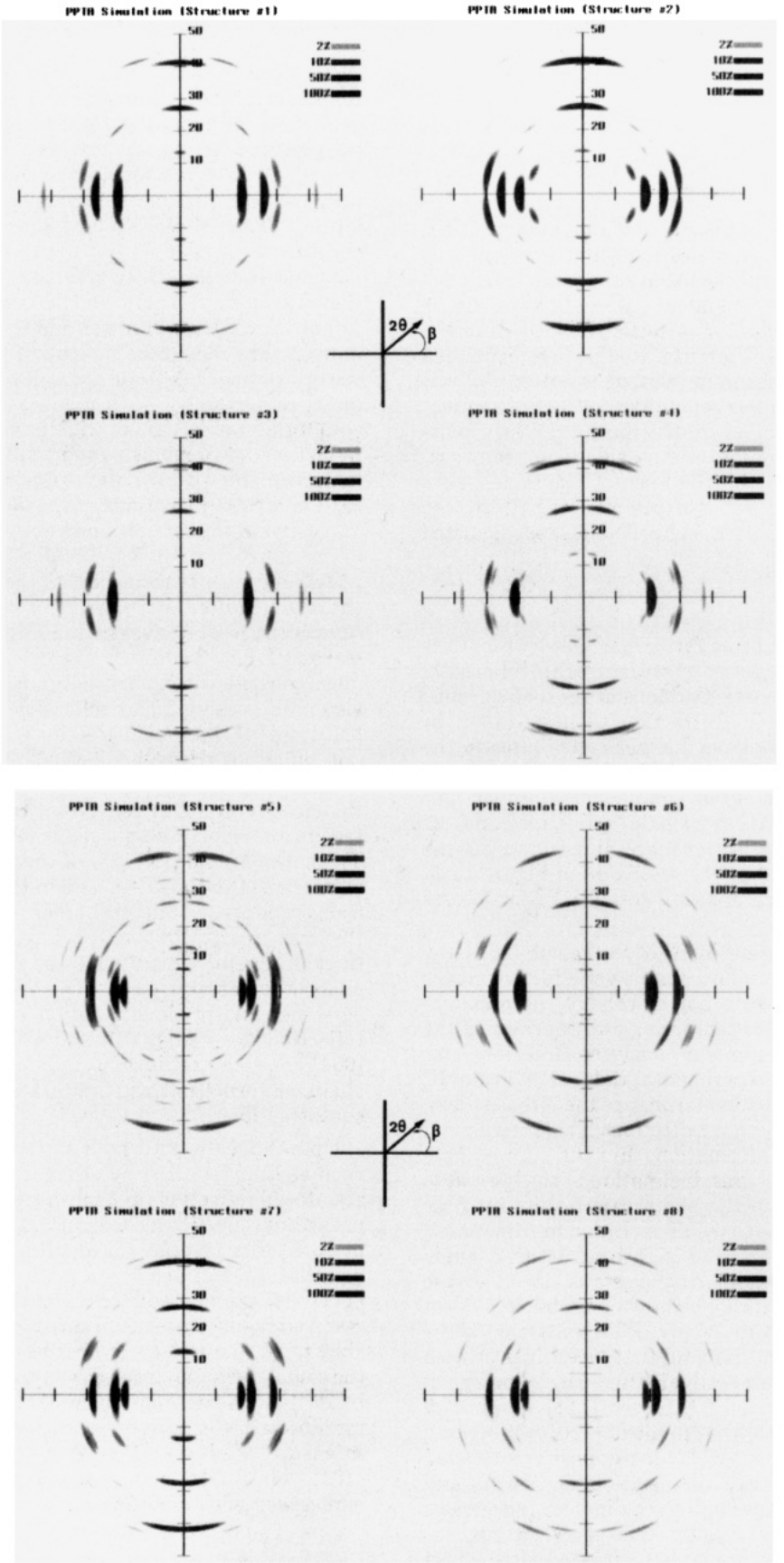

Figure 4. Calculated WAXS fiber diagram for PPTA fiber; a–h correspond to structures 1–8.

position and intensity of the remaining significant reflections is encouraging. Structure 3 most closely approximates the experimental pattern. One notes that in the simulated pattern for structure 4, the [00*l*] reflections lie off the meridian; this is due to the deviation in the crystallographic angle β from 90°, indicative of a slight shift between successive sheets of hydrogen-bonded chains. The annealed fiber appears to exhibit characteristics of both polymorphic forms. The reflection "families" listed in Table IV may be compared directly with the integrated

Table III
Experimentally Determined Reflections in PPTA Fibers Produced in This Work and Those Reported in the Literature for Modifications I and II[a]

as-spun fiber[f]			annealed fiber[f]			modification I[d]			modification II[e]		
2θ	β	I	2θ	β	I	2θ	β^b	I	2θ	β^b	I
			13.7	84	3	13.7	m	7			
17.9	0	31							17.4	e	s
			20.4	0	81	20.5	e	81			
						21.7	g	8			
22.6	0	100	22.5	0	100	22.6	e	100	22.2	e	vs
27.7	0	45									
28.4	82	13	28.0	86	12	27.7	m	30	27.9	m	m
			29.1	13	23	29.3	g	14	*c*	g	m
			29.8	74	5						
			33.4	57	5						
39.2	72	8									
41.0	29	9	37.3	23	6	37.4	g	4			
			38.4	0	10	38.5	e	4			
43.7	85	35	43.4	85	26	42.0	m	35	*c*	m	m
			45.6	80	15	43.6	g	11			
49.0	15	8				50.0	g	4			
			49.9	0	8	46.1	e	1			
						47.2	g	1			

[a] $\lambda = 1.542$ Å. [b] e, m, and g refer to equatorial, meridional, and general reflections, respectively, since azimuthal angles of reflection are not reported. [c] The observed *d* spacing is not reported. [d] Northolt, 1974. [e] Haraguchi et al., 1979. [f] Corresponds to 3.2 draw-down ratio fiber from trial 2 (Table II).

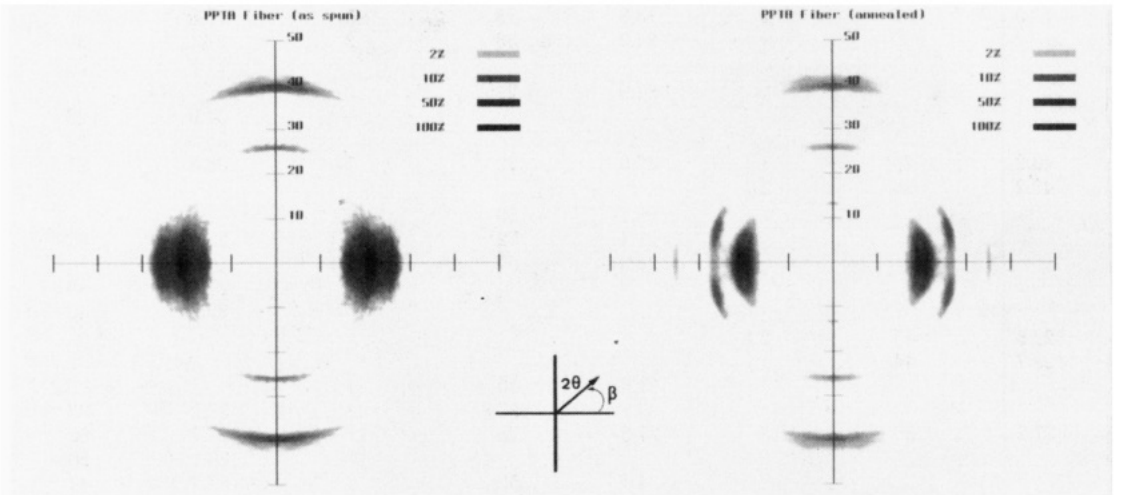

Figure 5. Representative X-ray fiber patterns for PPTA fibers spun during the course of this work: (a) as-spun fiber produced at a nominal draw-down ratio of 3.2; (b) same fiber after annealing for 2 s at 500 °C.

intensities for the annealed fiber listed in Table III, deduced from the two-dimensional Gaussian deconvolution procedure. The major reflections are represented in each calculated structure, while the minor reflections could derive from the presence of either or both possible contributors. The weaker meridional reflections predicted by simulation may be traced to the distortion, dictated by local packing constraints, of the 2_1 screw symmetry of the chain conformation.

The same trend in structure transformation was followed by using IR spectroscopy, with particular attention paid to the band shifts from 630 to 673 cm^{-1} and from 720 cm to 730 cm^{-1}, reported by Haraguchi et al.[33] to signal the transition from modification II to modification I. However, our IR data were not sensitive to such a transition upon annealing. Rather, we observe an obvious absorption at 720 cm^{-1}, characteristic of modification II, in both as-spun and annealed fibers, despite the clear predominance suggested by the X-ray results of modification I over modification II in the annealed fibers. The breadth of the absorption band between 600 and 690 cm^{-1} prevented us from drawing any conclusions about a band shift in this range as the result of annealing.

VII. Conclusions

On the basis of our simulation results described in detail in the previous paper and comparison of these with experimental X-ray results from the literature and our own laboratory, we suggest that PPTA, depending upon its processing history, may consist of an agglomeration of crystalline polymorphs, the relative occurrences of which are process dependent and may be altered by annealing and other postspinning techniques. These polymorphs are energetically similar and consists of aligned chains rearranged into hydrogen-bonded sheets which may then pack in several viable geometries. The use of molecular simulation provides a convenient means to anticipate the natures of the several crystal structures possible and provides one with suitable starting points for analyzing experimental X-ray data. Even more significant is the possibility this creates for studying data from mixed crystal systems, in that one can begin to deconvolute the experimental data and identify those reflections belonging to each polymorph for further refinement. While the predicted angular positions of reflections may differ measurably from observed peak positions, the relative dis-

Table IV
Summary of X-ray Reflections in Molecular Simulation Structures of PPTA

	structure 3			structure 4			structure 5		
hkl	2θ	β	*I*	2θ	β	*I*	2θ	β	*I*
010							18.4	0	49
110	21.0	0	74	21.0	0	50			
1$\bar{1}$0	20.5	0	23	21.2	0	21			
200	21.4	0	100	21.5	0	100	21.3	0	100
210							28.2	0	11
2$\bar{1}$0							28.3	0	6
310	37.7	0	7	37.3	0	4			
3$\bar{1}$0	36.7	0	1	37.7	0	1			
001							6.9	80	9
$\bar{1}$01				13.8	29	3			
011				19.0	21	2	18.5	21	1
0$\bar{1}$1				19.9	20	4	20.8	19	1
111	22.1	18	1						
$\bar{1}$11							21.5	18	2
$\bar{1}\bar{1}$1	22.1	18	2				23.4	17	4
201	22.5	18	2						
$\bar{2}$01	22.5	18	2						
211	29.2	13	4	27.6	14	2	28.5	14	6
$\bar{2}$11	28.4	14	5	30.0	13	6			
2$\bar{1}$1	28.5	14	5	28.6	14	4	29.9	13	3
$\bar{2}\bar{1}$1	29.2	13	4	30.3	13	7	29.9	13	5
121				38.0	10	1			
$\bar{3}$01				34.7	11	2			
002	13.5	90	5	13.8	78	5	13.8	80	5
1$\bar{1}$2				24.9	33	2	27.1	30	2
$\bar{1}$12							27.2	30	3
$\bar{2}$02				27.9	29	2			
302							34.9	23	1
$\bar{3}$02							35.3	23	2
312	40.2	20	1	37.0	22	1	38.5	21	1
$\bar{3}\bar{1}$2	40.2	20	1						
013				26.7	50	2			
103				21.4	72	2	23.1	62	4
$\bar{1}$03				25.3	54	1			
113							27.3	48	4
$\bar{1}\bar{1}$3							32.2	40	1
203	29.8	43	2						
$\bar{2}$03	29.7	44	1						
213				31.6	40	2			
303				35.1	35.8	2	38.2	33	1
004	27.2	90	13	27.8	78	17	27.7	80	4
0$\bar{1}$4							36.1	50	1
1$\bar{1}$4				34.5	52	3	37.7	47	1
005							34.9	80	2
015							36.6	70	1
006	41.3	90	9	42.3	78	17	42.1	80	4
106	42.8	75	4						
$\bar{1}$06	42.8	75	4						
016							43.1	74	7
116				44.3	69	3.4			
206				43.7	72	2			

tribution of peak positions and intensities suggests the fundamental accuracy and utility of the predictive method; the results from such analysis may serve as starting points for quantitative refinement of the structural description where quality of experimental data warrants and can provide valuable insight into the source of structure formation.

Acknowledgment. We gratefully acknowledge the financial support of a Graduate Fellowship to G.C.R. from the National Science Foundation and grants from the Office of Naval Research and the Materials Research Laboratory at the Massachusetts Institute of Technology. Partial support of U.W.S. through the Bayer Professorship to the Department of Chemical Engineering at the Massachusetts Institute of Technology and a Fulbright Senior Research Scholarship to C.D.P. are also greatly appreciated.

References and Notes

(1) Rutledge, G. C.; Suter, U. W. *Macromolecules*, preceding paper in this issue.
(2) Kwolek, S. U.S. Patent 3 671 542, June 20, 1972.
(3) Morgan, R. J.; Allred, R. E. *Reference Book for Composites Technology*; Lee, S. M., Ed., in press.
(4) Chatzi, E. G.; Koenig, J. L. *Polym.-Plast. Technol. Eng.* **1987**, *26* (3&4), 229.
(5) Kwolek, S.; Memeger, W.; Van Trump, J. E. *International Symposium on Polymers for Advanced Technology*; Lewin, M., Ed.; International Union of Pure and Applied Chemistry: 1987, p 421.
(6) Wilfong, R. E.; Zimmerman, J. *J. Appl. Polym. Sci., Polym. Symp.* **1977**, *31*, 1.
(7) Jorgensen, W. L.; Swenson, C. J. *J. Am. Chem. Soc.* **1985**, *107*, 569.
(8) Ramachandran; Mitra, *J. Mol. Biol.* **1976**, *197*, 85.
(9) Arpin, M.; Strazielle, C. *Polymer* **1977**, *18*, 591.
(10) Zero, K.; Aharoni, S. M. *Macromolecules* **1987**, *20*, 1957.
(11) Millaud, B.; Strazielle, C. *Makromol. Chem.* **1978**, *179*, 1261.
(12) Flory, P. J. *Molecular Theory of Liquid Crystals*; Advances in Polymer Science 59; Academic Press: New York, 1984.

(13) Flory, P. J.; Ronca, G. *Mol. Cryst. Liq. Cryst.* **1979**, *54*, 289.
(14) Flory, P. J.; Ronca, G. *Mol. Cryst. Liq. Cryst.* **1979**, *54*, 311.
(15) Flory, P. J. *Proc. R. Soc. London* **1956**, *A234*, 60.
(16) Aoki, H.; Coffin, D. R.; Hancock, T. A.; Harwood, D.; Lenk, R. S.; Fellers, J. F.; White, J. L. *J. Polym. Sci., Polym. Symp.* **1978**, *65*, 29.
(17) Erman, B.; Flory, J. P.; Hummel, J. P. *Macromolecules* **1980**, *13*, 484.
(18) Blades, H. U.S. Patent 3 767 756, Oct 23, 1973.
(19) Blades, H. U.S. Patent 3 869 430, Mar 4, 1975.
(20) Hancock, T. A.; Spruiell, J. E.; White, J. L. *J. Appl. Polym. Sci.* **1977**, *21*, 1227.
(21) White, J. L.; Fellers, J. F. *J. Appl. Polym. Sci., Appl. Polym. Symp.* **1978**, *33*, 137.
(22) Valenti, B.; Alfonso, G. C.; Ciferri, A.; Giordani, P. *J. Appl. Polym. Sci.* **1981**, *26*, 3643.
(23) Conio, G.; Bruzzone, R.; Ciferri, A.; Bianchi, E.; Tealdi, A. *Polym. J.* **1987**, *19*, 757.
(24) Chung, T. *J. Polym. Sci., Polymer Lett.* **1986**, *24*, 299.
(25) Kwolek, S. L.; Morgan, P. W.; Schaefgen, J. R.; Gulrich, L. W. *Macromolecules* **1977**, *10* (6), 1390.
(26) Dobb, M. G.; Johnson, D. J.; Saville, B. P. *J. Polym. Sci., Polym. Phys. Ed.* **1977**, *15*, 2201.
(27) Dobb, M. G.; Johnson, D. J.; Saville, B. P. *J. Polym. Sci., Polym. Symp.* **1977**, *58*, 237.
(28) Panar, M.; Avakian, P.; Blume, R. C.; Gardner, K. H.; Gierke, T. D.; Yang, H. H. *J. Polym. Sci., Polym. Phys. Ed.* **1983**, *21*, 1955.
(29) Northolt, M. G.; Van Aartsen, J. J. *J. Polym. Sci., Polym. Symp.* **1977**, *58*, 283.
(30) Barton, R. *J. Macromol. Sci., Phys.* **1985–1986**, *B24*, 119.
(31) Hindeleh, A. M.; Halim, N. A.; Ziq, K. A. *J. Macromol. Sci., Phys.* **1984**, *B23* (3), 289.
(32) Northolt, M. G. *Eur. Polym. J.* **1974**, *10*, 799.
(33) Haraguchi, K.; Kajiyama, T.; Takayanagi, M. *J. Appl. Polym. Sci.* **1979**, *23*, 915.
(34) Gardner, K. H.; Matheson, R. R.; Avakian, P.; Chia, Y. T.; Gierke, T. D. *Polymers for Fibers and Elastomers*; Arthur, J. C., Ed.; American Chemical Society: Washington, DC, 1984; p 91.
(35) Penn, L.; Newey, H. A.,; Chiao, T. T. *J. Mater. Sci.* **1976**, *11*, 190.
(36) Morgan, R. J.; Pruneda, C. O.; Steele, W. J. *J. Polym. Sci., Polym. Phys. Ed.* **1983**, *21*, 1757.
(37) Morgan, R. J.; Mones, E. T.; Steele, W. J.; Deutscher, S. B. *Polym. Prepr. (Am. Chem. Soc., Div. Polym. Chem.)* **1980**, *21* (2), 264.
(38) Jaffe, M.; Jones, R. S. *High Performance Aramid Fibers*; *Handbook of Fiber Science and Technology*; Lewin, M., Preston, J., Eds.; Marcel Dekker: New York, 1985; Vol. III, p 349.
(39) Alexander, L. E. *X-Ray Diffraction Methods in Polymer Science*; Wiley-Interscience: New York, 1969.
(40) de Wolff, P. M. *J. Polym. Sci.* **1962**, *60*, S34.
(41) Haraguchi, K.; Kajiyama, T.; Takayanagi, M. *J. Appl. Polym. Sci.* **1979**, *23*, 903.
(42) English, A. D. *J. Polym. Sci., Polym. Phys. Ed.* **1986**, *24*, 805.